Adjoint Multi-Start Based Estimation of Cardiac Hyperelastic Material Parameters using Shear Data

**Gabriel Balaban · Martin S. Alnæs ·
Joakim Sundnes · Marie E. Rognes**

Abstract Cardiac muscle tissue during relaxation is commonly modelled as a hyperelastic material with strongly nonlinear and anisotropic stress response. Adapting the behavior of such a model to experiment or patient data gives rise to a parameter estimation problem which involves a significant number of parameters. Gradient-based optimization algorithms provide a way to solve such nonlinear parameter estimation problems with relatively few iterations, but require the gradient of the objective functional with respect to the model parameters. This gradient has traditionally been obtained using finite differences, the calculation of which scales linearly with the number of model parameters, and introduces a differencing error. By using an automatically derived adjoint equation, we are able to calculate this gradient more efficiently, and with minimal implementation effort. We test this adjoint framework on a least squares fitting problem involving data from simple shear tests on cardiac tissue samples. A second challenge which arises in gradient-based optimization is the dependency of the algorithm on a suitable initial guess. We show how a multi-start procedure can alleviate this dependency. Finally, we provide estimates for the material parameters of the Holzapfel and Ogden strain energy law using finite element models together with experimental shear data.

G. Balaban, M. S. Alnæs, J. Sundnes, M. E. Rognes
Simula Research Laboratory
P.O. Box 134 1325 Lysaker, Norway
Tel.: +47 67 82 82 00
Fax: +47 67 82 82 01
E-mail: gabrib@simula.no

G. Balaban, J. Sundnes
Department of Informatics
University of Oslo
P.O. Box 1080 Blindern 0316 Oslo, Norway

M. E. Rognes
Department of Mathematics
University of Oslo
P.O. Box 1053 Blindern 0316 Oslo, Norway

1 Introduction

The personalization of computational models in cardiology is a key step towards making models useful in the clinic. A computational model, once properly calibrated, has the potential to forecast cardiac function and disease, and can aid in planning treatments and therapies. To describe the mechanical function of the heart, the passive elasticity of the muscle tissue needs to be represented. Personalizing the effects of this elasticity in a computational model is typically accomplished by tuning a set of material parameters so that the output of the model fits observed data. Gradient-based optimization algorithms have successfully been used in the past to automatically perform the parameter tuning at an organ scale [2,28]. In these studies, the gradient of the objective functional is approximated using one-sided finite differences.

Compared to using a global optimization method, local gradient-based methods have the advantage of using relatively few optimization iterations. This is an important consideration when optimizing organ scale finite element models, for which running a single forward model can take hours or days. On the other hand, a disadvantage of using local optimization methods is the fact that they can converge to local, globally suboptimal, minima. One way to combine the speed of a local optimization with the robustness of a global optimization is to use the multi-start method. In this method, many local optimizations are run starting from various points in parameter space and the best fitting solution of the group is taken to be the global optimum.

Another popular approach to parameter fitting is the reduced order unscented Kalman filter. This approach was successfully used to fit a transversely isotropic passive mechanics model to synthetic data [30], to partially calibrate a multi-physics model [21], and to estimate regional contractility parameters [6]. Note however that the use of both unscented Kalman filtering and finite differences carries a computational cost that increases with the number of model parameters.

Assuming there are k parameters to be estimated, an unscented Kalman filter with a minimal sigma-point configuration requires $k + 1$ model evaluations at a single time level for each assimilated data point. An evaluation of a finite difference derivative on the other hand requires $k + 1$ runs of the model throughout the full span of model configurations considered.

In contrast to these two techniques, the adjoint approach computes the objective functional gradient via the solution to an adjoint equation, which involves only a single solve of a linearized system for any number of model parameters. Thus, for models involving many parameters, either due to model complexity or spatiotemporal parameter variation, the adjoint approach offers a computationally attractive approach for parameter estimation.

There are some previous results involving adjoint equations and cardiac elasticity. Sundar et al. (2009) developed a framework for the estimation of wall motion based on cine-MRI images and adjoint inversion [25], and Delingette et al. (2012) used an adjoint equation to estimate contractility parameters [8]. However, both of these studies involve linear and isotropic elasticity models, which represent a significant simplification of the orthotropic and highly nonlinear behavior reported in the contemporary cardiac mechanics literature [7,9,16].

One reason why it is difficult to use an adjoint equation with modern nonlinear anisotropic models is the complexity required in deriving and implementing code for the solution of the adjoint problem. In order to resolve this issue, we make use of an automatic framework for generating adjoint code [10]. Here, we use this adjoint framework to estimate the material parameters of an invariant-based orthotropic myocardial strain energy law (the Holzapfel-Ogden model) [16]. This law is embedded here in an incompressible finite element framework, and we use the raw data from a simple shearing experiment [9] as a target for optimization. These data have previously been used to estimate material parameters for a variety of other strain energy functions using a finite element framework, but with a gradient obtained using finite differences [23,24]. The material parameters of the particular strain energy density that we are using have also been previously estimated using digitized data based on Figure 6 of [9], and a homogeneous deformation model [13,16,27]. Our study is however the first to use the adjoint approach for the estimation of cardiac hyperelasticity parameters and the first to provide optimized material parameters for the incompressible Holzapfel-Ogden model for non-homogeneous deformations.

The rest of this paper is organized as follows. In Section 2 we describe the variational formulation of the elasticity model, the optimization problem for identifying the material parameters, and how the adjoint gradient formula can be used to calculate a functional gradient. In Section 3 we describe the verification of the forward and inverse solvers, present timings to show the efficiency of the adjoint method, and show the results of parameter estimations. Finally, we test a multi-start optimization method in order to reduce the dependence of the gradient-based algorithm on the choice of initial parameter set. We conclude by discussing our findings in Section 4, and drawing some conclusions in Section 5.

2 Mathematical models and methods

We shall use the notion of the directional derivative frequently throughout. For a functional $f : Y \to \mathbb{R}$ for some vector space Y, we define the directional derivative of f with respect to the argument named $\mathbf{y}$ in the direction $\delta \mathbf{y}$:

$$D_{\mathbf{y}} f(\mathbf{y})[\delta \mathbf{y}] \equiv \frac{\partial}{\partial \epsilon} f(\mathbf{y} + \epsilon \, \delta \mathbf{y}) \Big|_{\epsilon = 0},$$

with shortcut notation $D_{\delta \mathbf{y}} f(\mathbf{y}) \equiv D_{\mathbf{y}} f(\mathbf{y})[\delta \mathbf{y}]$.

2.1 Hyperelasticity model

Let $\Omega \subset \mathbb{R}^3$ be an open and bounded domain with coordinates $\mathbf{X}$ and boundary $\partial\Omega$, occupied by an incompressible hyperelastic body. We consider the quasi-static regime of a body undergoing a large deformation $\mathbf{x} = \mathbf{x}(\mathbf{X})$ and are interested in finding the displacement $\mathbf{u} = \mathbf{u}(\mathbf{X}) = \mathbf{x} - \mathbf{X}$ and the hydrostatic pressure $p = p(\mathbf{X})$ that minimize the incompressible strain energy $\Pi = \Pi(\mathbf{u}, p, \mathbf{m})$:

$$\Pi(\mathbf{u}, p, \mathbf{m}) = \int_{\Omega} \psi(\overline{\mathbf{C}}, \mathbf{m}) + p(J - 1) \, \mathrm{dx} \tag{1}$$

over the space of admissible displacements and pressures satisfying any given Dirichlet boundary conditions. In (1), $J = \det \mathbf{F}$, where $\mathbf{F} = \nabla \mathbf{x} = \nabla \mathbf{u} + \mathbf{I}$ denotes the deformation gradient, $\mathbf{I}$ is the identity tensor in $\mathbb{R}^3$, $\overline{\mathbf{C}} = J^{-\frac{2}{3}} \mathbf{F}^T \mathbf{F}$ denotes a volume-preserving right Cauchy-Green strain tensor, ψ denotes an isochoric strain energy density, and $\mathbf{m}$ is a set of material parameters.

The incompressible Holzapfel and Ogden hyperelasticity model [16] describes large deformations and stresses in cardiac tissue via the following energy density ψ:

$$\begin{aligned}
\psi(\overline{\mathbf{C}}, \mathbf{m}) = {} & \frac{a}{2b} \left(\exp\left[b(I_1(\overline{\mathbf{C}}) - 3) \right] - 1 \right) \\
& + \sum_{i=f,s} \frac{h(I_{4i}(\overline{\mathbf{C}}))a_i}{2b_i} \left(\exp\left[b_i(I_{4i}(\overline{\mathbf{C}}) - 1)^2 \right] - 1 \right) \\
& + \frac{a_{fs}}{2b_{fs}} \left(\exp\left[b_{fs} I_{8fs}^2(\overline{\mathbf{C}}) \right] - 1 \right).
\end{aligned} \tag{2}$$

Here f, s denote fiber and sheet directions, respectively; $h(x)$ is a Heaviside function with a jump at $x = 1$, and the material parameters are

$$\mathbf{m} = (a, b, a_f, b_f, a_s, b_s, a_{fs}, b_{fs}). \tag{3}$$

Moreover, $I_1, I_{4s}, I_{4f}, I_{8fs}^2$ are rotation invariant functions given by

$$\begin{aligned}
I_1(\overline{\mathbf{C}}) &= \mathrm{tr}\,\overline{\mathbf{C}} \\
I_{4i}(\overline{\mathbf{C}}) &= \mathbf{e}_i \cdot \overline{\mathbf{C}} \mathbf{e}_i \quad i = f, s \\
I_{8fs}(\overline{\mathbf{C}}) &= \mathbf{e}_s \cdot \overline{\mathbf{C}} \mathbf{e}_f
\end{aligned}$$

where tr denotes the tensor trace and $\mathbf{e}_f, \mathbf{e}_s$ denote unit vectors pointing in the local myocardial fiber and sheet directions [16]. The strain energy density ψ is rotation-invariant, and polyconvex if $\mathbf{m} > 0$ [16].

The Euler-Lagrange equations for the minimizing displacement $\mathbf{u}$ and pressure p of (1) read: for given $\mathbf{m}$, find $\mathbf{w} = (\mathbf{u}, p)$ such that

$$R(\mathbf{w}, \mathbf{m}; \delta\mathbf{w}) \equiv D_{\delta\mathbf{u},\delta p} \Pi(\mathbf{u}, p) = 0, \tag{4}$$

for all admissible virtual variations $\delta\mathbf{w} = (\delta\mathbf{u}, \delta p)$. Inserting the total potential energy from (1) and taking the directional derivative, we obtain

$$D_{\delta\mathbf{u},\delta p}\Pi(\mathbf{u}, p, \mathbf{m}) = \int_{\Omega} \left(\left(J\mathbf{F}^{-T} + \frac{\partial\psi(\overline{\mathbf{C}}, \mathbf{m})}{\partial\mathbf{F}} \right) : \nabla\delta\mathbf{u} + (J-1)\delta p \right) \, \mathrm{dx}.$$

2.2 Parameter estimation as a PDE-constrained optimization problem

In the general case, the passive material parameters $\mathbf{m}$ entering the constitutive relationship (2) are not known. In order to estimate these parameters from data, we propose to use a numerical approximation in combination with a gradient-based optimization algorithm in which the gradients are computed via an adjoint model. The optimization algorithm seeks to minimize the misfit between model output and observations. Denoting the misfit functional by $I = I(\mathbf{w}(\mathbf{m}), \mathbf{m})$, the optimization problem reads:

$$\min_{\mathbf{m}} I(\mathbf{w}(\mathbf{m}), \mathbf{m}) \qquad \text{subject to} \qquad R(\mathbf{w}, \mathbf{m}; \delta\mathbf{w}) = 0 \quad \forall\delta\mathbf{w} \in W, \quad (5)$$

together with suitable Dirichlet boundary conditions on $\mathbf{w}$. We also require that $\mathbf{m} > 0$ to ensure the functional (1) is polyconvex [16]. For notational convenience we will sometimes use the reduced formulation of the misfit functional and its gradient with respect to the material parameters $\mathbf{m}$. In particular, we introduce the reduced functional $\hat{I}$ and its gradient defined via:

$$\begin{aligned}
\hat{I}(\mathbf{m}) &\equiv I(\mathbf{w}(\mathbf{m}), \mathbf{m}), \\
\nabla\hat{I}(\mathbf{m}) &\equiv \frac{D}{D\mathbf{m}} I(\mathbf{w}(\mathbf{m}), \mathbf{m}).
\end{aligned} \qquad (6)$$

In our numerical experiments we use limited memory BFGS (Broyden, Fletcher, Goldfarb, and Shanno) with bound constrains [5], as implemented in [31] and wrapped in the package SciPy [18] in order to solve (5).

2.3 Multi-start Optimization

A common challenge with gradient-based algorithms is that the solution obtained depends on the choice of initialization point for the algorithm. Moreover, the optimized solution may be a local minimum only and not necessarily a global minimum. One way to attack these issues is to run many optimizations from randomly chosen initial parameter points, and to chose the resulting optimized material parameter set that gives the best fit. This method is often referred to as multi-start optimization [4] and is an example of combining global and local optimization.

Due to the presence of exponential functions in the strain energy (2), it is possible for calculated stresses to become very large, which may result in convergence issues for the numerical solution of the Euler-Lagrange equation (4). This can easily occur if several material parameters have large values. In order

to minimize this problem we have designed a procedure to generate random initial guesses which limits the number of large material parameter values while still allowing for a large range of initial possible values for each parameter. The procedure works as follows: first set a maximum parameter value P_{max}. Then choose n (with $n = 8$ in our case) points from a uniform distribution defined over the interval $[0, P_{max}]$. The parameter values are then set to be the distances between successive randomly drawn points.

2.4 Computing the functional gradient via the adjoint solution

Gradient-based optimization algorithms in general, and the BFGS algorithm in particular, rely on the total derivative of the objective functional (6). By introducing an *adjoint* state variable, this derivative may be computed efficiently. We summarize this result below. Our presentation is based on [15], and is adapted here to the solid mechanics setting.

We define three abstract spaces W, M, and Φ, where W is the space of all possible solutions to the variational equation (4) which also satisfy any given Dirichlet boundary conditions, M is the material parameter vector space, and Φ is the space of virtual variations. The Lagrangian $L : W \times M \times \Phi \to \mathbb{R}$ is defined as:

$$L(\mathbf{w}, \mathbf{m}, \phi) = I(\mathbf{w}, \mathbf{m}) - R(\mathbf{w}, \mathbf{m}; \phi). \tag{7}$$

For all $\mathbf{m} \in M$, $\mathbf{w} \in W$ solving the state equation (4), we have

$$\frac{D}{D\mathbf{m}} R(\mathbf{w}(\mathbf{m}), \mathbf{m}; \phi) = 0,$$

such that the total derivatives of I and L coincide,

$$\frac{D}{D\mathbf{m}} I(\mathbf{w}(\mathbf{m}), \mathbf{m}) = \frac{D}{D\mathbf{m}} L(\mathbf{w}(\mathbf{m}), \mathbf{m}, \phi). \tag{8}$$

If we (can) choose $\phi \in \Phi$ such that

$$D_{\mathbf{w}} L(\mathbf{w}, \mathbf{m}, \phi)[\delta\mathbf{w}] = 0 \tag{9}$$

for all $\delta\mathbf{w} \in W$, which in particular includes $\delta\mathbf{w} = D_{\delta\mathbf{m}}\mathbf{w}(\mathbf{m})$, the total derivative of L with respect to $\mathbf{m}$ in the direction $\delta\mathbf{m}$ simplifies as follows using the chain rule:

$$\frac{D}{D\mathbf{m}} L(\mathbf{w}(\mathbf{m}), \mathbf{m}, \phi)[\delta\mathbf{m}] = D_{\mathbf{w}} L(\mathbf{w}, \mathbf{m}, \phi)[D_{\delta\mathbf{m}}\mathbf{w}(\mathbf{m})] + D_{\delta\mathbf{m}} L(\mathbf{w}, \mathbf{m}, \phi)$$
$$= D_{\delta\mathbf{m}} L(\mathbf{w}, \mathbf{m}, \phi) \tag{10}$$

Then, for any infinitesimal variation in the material parameters $\delta\mathbf{m}$, combining (8), (10), and (7) yields an efficient evaluation formula, not requiring

derivatives of the state variable $\mathbf{w}$ with respect to the material parameters $\mathbf{m}$, for the total derivative of I:

$$\frac{D}{D\mathbf{m}}I(\mathbf{w}(\mathbf{m}), \mathbf{m}) = D_{\delta\mathbf{m}}I(\mathbf{w}, \mathbf{m}) - D_{\delta\mathbf{m}}R(\mathbf{w}, \mathbf{m}, \phi). \quad (11)$$

We still need to compute ϕ. By defining the form $R_{\mathbf{w}}$ and its adjoint $R_{\mathbf{w}}^*$,

$$R_{\mathbf{w}}(\mathbf{w}, \mathbf{m}; \delta\mathbf{w}, \phi) \equiv D_{\delta\mathbf{w}}R(\mathbf{w}, \mathbf{m}; \phi),$$
$$R_{\mathbf{w}}^*(\mathbf{w}, \mathbf{m}; \phi, \delta\mathbf{w}) \equiv R_{\mathbf{w}}(\mathbf{w}, \mathbf{m}; \delta\mathbf{w}, \phi),$$

we can rewrite (9) as

$$D_{\mathbf{w}}L(\mathbf{w}, \mathbf{m}, \phi)[\delta\mathbf{w}] = D_{\mathbf{w}}I(\mathbf{w}, \mathbf{m})[\delta\mathbf{w}] - R_{\mathbf{w}}^*(\mathbf{w}, \mathbf{m}; \phi, \delta\mathbf{w}) = 0,$$

and thus recognize the adjoint equation: given $\mathbf{m}$, $\mathbf{w}$, find $\phi \in \Phi$ such that

$$R_{\mathbf{w}}^*(\mathbf{w}, \mathbf{m}; \phi, \delta\mathbf{w}) = D_{\mathbf{w}}I(\mathbf{w}, \mathbf{m})[\delta\mathbf{w}] \quad (12)$$

for all $\delta\mathbf{w} \in W$.

In summary, the adjoint-based gradient evaluation formula is: given $\mathbf{m}$, first compute $\mathbf{w}$ by solving the state equation (4), next compute ϕ by solving (12), and finally evaluate (11).

2.5 Description of shearing experiments

We aim to optimize the material parameters of the Holzapfel-Ogden model (2) with respect to target experimental data, in particular data resulting from an earlier set of simple shearing experiments [9]. In these experiments, 6 pig hearts were extracted. From each heart, three adjacent 3mm $\times$ 3mm $\times$ 3mm cubic blocks were cut in such a way that the sides of the cubes were aligned with the local myocardial fiber and sheet directions. A device held two opposing faces of each cube between two plates using an adhesive. The top plate was displaced in order to put each specimen in simple shear. For each specimen 6 different modes of shear were tested. These modes are described using the F, S, N coordinate system, which refer to the myocardial fiber, sheet and sheet normal directions, respectively. Each mode is denoted by two letters, where the first defines the normal of the face of the cube that is being displaced, and the second refers to the direction of displacement. These 6 modes are FS, FN, SF, SN, NF, NS.

In order to remove the effects of strain softening, preliminary displacements were applied to the tissue samples until no further softening was observed. After that, displacements were once again applied, and the forces in the shear direction were measured on the top plate. These measurements were taken for circa $200 - 250$ various states of shear per mode.

In Figure 1 we display the stress-strain relations that were obtained during the shearing experiments [9]. As we only consider the elastic, and not the viscous, material response only the loading curves are displayed. Furthermore

we observe that the experimentally obtained curves contain a high degree of symmetry through the line $y = -x$ and we have therefore chosen to use only the data for positive shear displacements. We can expect the same symmetry in the stresses computed by finite element models which use the strain energy (2) since changing the sign of the displacement map will change the sign of the resulting stresses but preserve their magnitude.

In our numerical experiments we use two data sets with reference to the numbering of [9]. The first is Data Set 6, and the second data is Data Set 2 with the SF and SN curves swapped. This swap and the choice of data sets are discussed further in Section 4. For clarity, we shall refer to Data Set 6 as "transversely isotropic" and Data Set 2 with the swap as "orthotropic", as the respective stress-strain curves are typical of materials of these types. For each mode, the prescribed shear displacement is modelled as a Dirichlet boundary condition for the displacement on the respective top and bottom faces in the respective direction.

2.6 Choice of objective functional

In order to estimate the passive material parameters of the Holzapfel-Ogden model, we make use of a least squares objective functional. This functional defines a distance from the model output to the data points of the shearing experiment, and we seek the material parameter set $\mathbf{m}$ that minimizes this. Before introducing our objective functional, we define the set of directions $\mathcal{D} = \{F, S, N\}$, referring to fiber, sheet and sheet normal directions. We also use the notation (i, j) to refer to a mode, with the index i referring to the normal of the face that is shifted, and j to the direction in which the shift occurs.

Our fit function is similar to that used in [22], and is given by

$$\hat{I}(\mathbf{m})^2 = \sum_{i \in \mathcal{D}} \sum_{j \in \mathcal{D}} \sum_{k=1}^{G} \omega_k \left(t_{\text{model}}^{i,j}(x_k, \mathbf{m}) - t_{\text{exper}}^{i,j}(x_k) \right)^2 \qquad (13)$$

In (13), $t_{\text{exper}}^{i,j}$ is the force measured during the experiment, and $t_{\text{model}}^{i,j}$ is the force generated by the finite element model at each prescribed shear displacement $x_k \in [0, X^{i,j}]$, where $X^{i,j}$ is the maximal prescribed displacement of the mode (i, j) in the experiment. Each x_k is chosen to be a Gauss point of a G-point rule defined over $[0, X^{i,j}]$, and ω_k is the value of the Gauss weight related to x_k. Explicitly, for mode (i, j) with top face $\partial \Omega_i$, $t_{\text{model}}^{i,j}$ is given by

$$t_{\text{model}}^{i,j}(x_k, \mathbf{m}) = \int_{\partial \Omega_i} \frac{\partial \psi(\mathbf{u}(x_k), \mathbf{m})}{\partial \mathbf{F}_{i,j}} \ \text{dS},$$

where $\mathbf{F}_{i,j} = \mathbf{e}_i \cdot \mathbf{F} \mathbf{e}_j$ the shear component of the deformation gradient.

Evaluating the inner loop of $\hat{I}$ requires solving (4) once for each given shear displacement x_j. The motion given by the calculated displacements is then
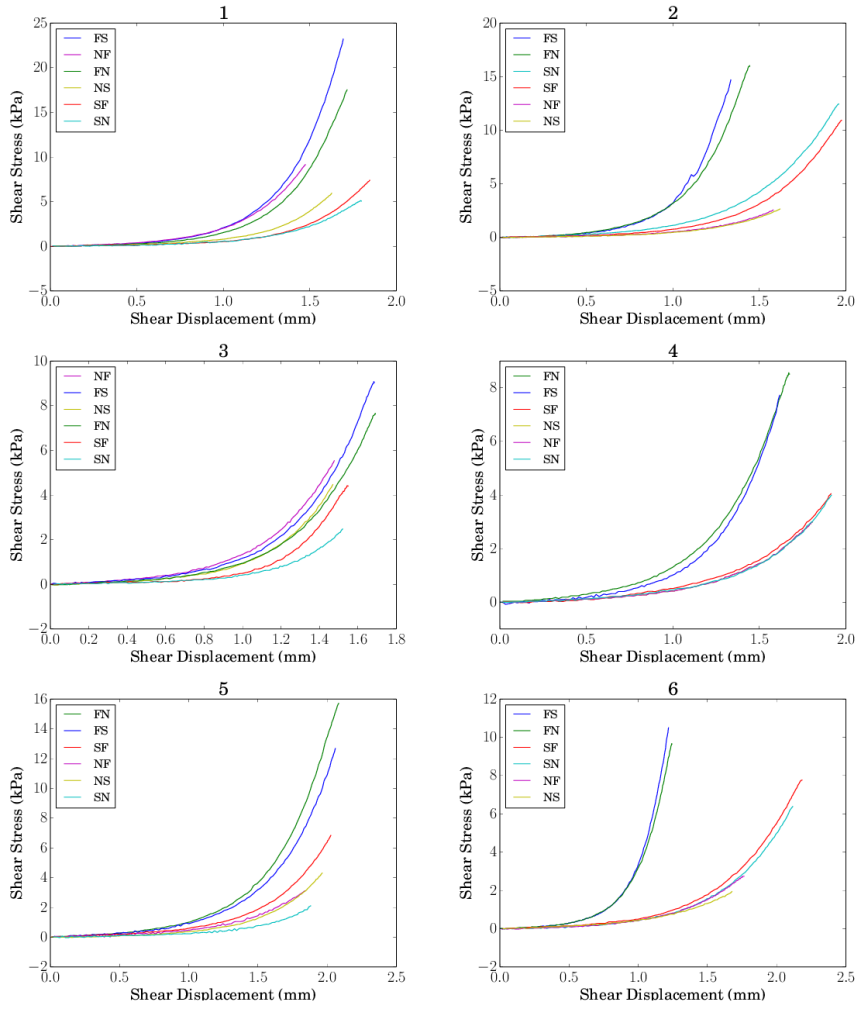
Fig. 1 Stress-strain relations, numbered 1 through 6, obtained from simple shearing experiments performed on 3mm × 3mm × 3mm cubes of myocardium extracted from 6 porcine hearts. The modes are ordered from highest to lowest stiffness in each experiment. The data originates from the study [9], but were not published in the subsequent article. In Experiment 4 the data for one of the NS-NF curves was copied into the other before we received it, so the two curves lie here on top of one another.

a quasi-static approximation of the motion undergone by the corresponding tissue in the shearing experiment.

Following [22], we evaluate the least squares fit (13) at G ($G = 9$) Gauss integration points, rather than for all 250 recorded points for each shear mode. At each Gauss point we obtain the corresponding shear stress by linearly interpolating between the two neighbouring stresses which were recorded in the experiments of Dokos et al. [9].

2.7 Finite element discretization of the hyperelasticity equations

We represent each tissue sample of the shearing experiments by a three-dimensional cube $\Omega = [0,3]^3$ (mm^3). An $N \times N \times N$ mesh of this cube was constructed by uniformly dividing the mesh into $N \times N \times N$ boxes and then subdividing the boxes into tetrahedra. On these geometries, we solve (4) and its adjoint, using a Galerkin finite element method with the Taylor-Hood finite element pair [17]; e.g. a continuous piecewise quadratic vector field for the displacement and a continuous piecewise linear scalar field for the pressure. For the solution of the nonlinear system of equations, we use a Newton trust region method. The absolute tolerance of the nonlinear solver was set to 10^{-10} in the numerical experiments below. Linear systems are solved by LU factorization.

Additionally, we model the case of a homogeneous deformation which corresponds to a linear displacement with a constant shear angle throughout the domain. Such a model can be represented by discretizing the cubes with a single layer of linear finite elements: the resulting displacement is completely determined by the prescribed boundary conditions. Figure 2 illustrates the two kinds of deformations on cube meshes.

The discrete variational formulation of the Euler-Lagrange equations is implemented using the FEniCS Project software [1, 20] and dolfin-adjoint [10]. From a FEniCS forward model, dolfin-adjoint automatically generates the symbolic adjoint system of equations and computes the functional gradient (11) using the adjoint solution. The FEniCS framework automatically generates and compiles efficient C++ code for the assembly of the relevant linear systems from the symbolic representations of both forward and adjoint equations, and solves the nonlinear and linear systems using e.g. PETSc [3]. With this setup, we observed that a typical solution of the Euler-Lagrange equation (4) takes 6 Newton iterations.
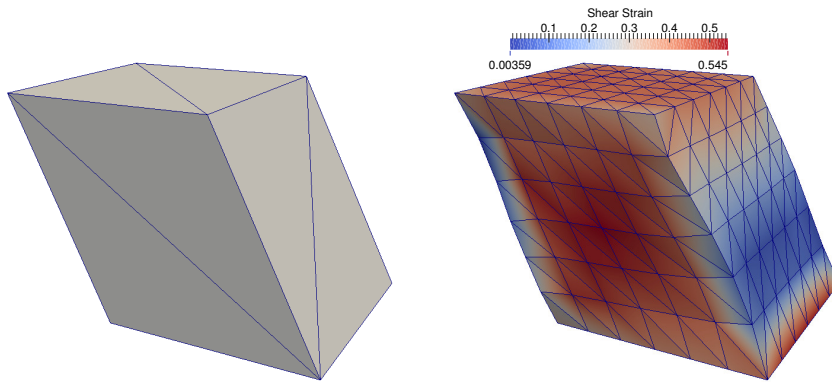
Fig. 2 Finite element representation of cubes of cardiac tissue undergoing simple shear in the NS mode. The bottom of the cube is fixed and the top displacement is given. Left: homogeneous deformation with a constant shear angle. Right: finite element solution on a $6 \times 6 \times 6$ mesh. The plot shows the value of the NS-component of the right Cauchy Green strain tensor $\mathbf{C}$.

3 Numerical Results

3.1 Verification

Each of the finite element, adjoint, and optimization solvers have been carefully verified, separately and combined, as follows. (i) The finite element solver was verified by the method of manufactured solutions, resulting in the expected second-order convergence for the displacement gradients [17]. (ii) We verified the computation of stresses in the finite element model by prescribing a homogeneous deformation and comparing the resulting numerically integrated top face shear stress values to analytically computed values. The analytic values were based on the calculations found in [16, Section 5a] and the numerical values were observed to match closely. (iii) We confirmed the correctness of the adjoint gradients by using Taylor's theorem: the expression

$$\hat{I}(\mathbf{m}) - \hat{I}(\mathbf{m}^*) - \nabla\hat{I}(\mathbf{m})(\mathbf{m} - \mathbf{m}^*) \tag{14}$$

converged to 0 at a rate of 2 in $(\mathbf{m} - \mathbf{m}^*)$, which can only be expected if $\nabla\hat{I}(\mathbf{m})$ is computed accurately.

3.2 Parameter estimation with synthetic data

Additionally, we verified the optimization solver by performing a synthetic data test. Using a known set of material parameters, we generated integrated stress values for all 6 shear modes used in the experiment [9] using the computational model, and used these synthetic data as target for optimization. As known material parameters, we used values 80% lower than the material

Table 1 Synthetic data test results. The first row (Initial) contains the material parameter values used to initialize the algorithm, while the second row (Target) contains the parameters that were used to generate the synthetic stresses. The rows marked 'Homogeneous' and 'Finite Element' contain optimized parameter values coming from homogeneous deformation and finite element models. These optimized values are matched perfectly by the optimized homogeneous model and very closely by the finite element model.

	a (kPa)	b	a_f (kPa)	b_f	a_s (kPa)	b_s	a_{fs} (kPa)	b_{fs}	I (mN)
Initial	0.059	8.023	18.472	16.026	2.481	11.120	0.216	11.436	
Target (80%)	0.047	6.418	14.778	12.821	1.985	8.896	0.173	9.149	
Homogeneous	0.047	6.418	14.778	12.821	1.985	8.896	0.173	9.149	4.611×10^{-8}
Finite Element	0.047	6.406	14.778	12.821	1.983	8.938	0.173	9.155	0.00082

parameter values used as the initial guess for the optimization. We performed this test using our two models for deformation. The first model assumed a homogeneous shear angle through the material and only numerically integrated the top face stress. The second model was a finite element model with a $1 \times 1 \times 1$ mesh. Since the displacement field is element-wise quadratic, this allows for more flexibility in the deformation field.

The results of this synthetic data test are presented in Table 1 and show that the optimization algorithm is able to recover the material parameters.

3.3 Parameter estimation with experimental stress data

In the following, we present the results of fitting the Holzapfel-Ogden strain energy law (2) using the objective function (13) and a limited memory BFGS optimizer with bound constraints. The BFGS algorithm makes use of the gradient of the objective functional which we obtain using the adjoint gradient formula (11).

As the numerical solution of the nonlinear Euler-Lagrange equation (4) easily fails to converge when a material parameter becomes too small, we set a lower bound of 1.0×10^{-2} on the components of $\mathbf{m}$ while optimizing finite element models. This bound was not necessary for the homogeneous deformation models as no Euler-Lagrange equation is solved. All optimizations were carried out until the optimizer was unable to further reduce the objective functional or an absolute tolerance of 1.0×10^{-6} in the objective functional was reached.

3.3.1 Material parameter estimation using a priori knowledge

The material parameters of the Holzapfel-Ogden model have previously been estimated using a homogeneous deformation model [16, Table 1, 2nd row]. We first used these values as the initial values for optimization of our homogeneous model targeting the transversely isotropic and orthotropic data sets. The optimized results are listed in Table 2 with the label Homogeneous.

	a (kPa)	b	a_f (kPa)	b_f	a_s (kPa)	b_s	a_{fs} (kPa)	b_{fs}	I (mN)	It.
Transversely Isotropic										
Homogeneous	0.876	4.219	97.828	30.093	2.002	4.191×10^{-5}	0.330	1.137	3.903	96
N = 1	0.060	16.941	30.484	29.556	2.110	0.264	0.036	0.884	5.553	90
N = 2	0.731	6.821	22.062	40.044	0.010	0.010	0.183	13.619	3.011	86
N = 4	0.775	6.955	21.640	39.866	0.010	0.010	0.218	13.654	2.857	12
N = 6	0.732	7.362	21.511	40.020	0.010	0.010	0.209	13.862	2.827	16
N = 8	0.736	7.363	21.507	40.019	0.010	0.010	0.201	13.862	2.833	5
Orthotropic										
Homogeneous	0.775	5.929	138.283	7.065	13.61	8.222×10^{-10}	1.037	2.304	7.057	178
N = 1	0.766	6.857	31.642	15.209	2.070	0.010	0.352	15.242	5.880	69
N = 2	1.041	6.553	29.371	15.982	1.741	0.010	0.118	23.294	4.563	59
N = 4	1.041	6.553	29.371	15.982	1.741	0.010	0.118	23.294	4.508	10

Table 2 Material parameters fitted to the orthotropic and transversely isotropic datasets for the Homogeneous and $N \times N \times N$ finite element models. I refers to the value of the objective functional. The number of optimization iterations, each consisting of functional and functional gradient evaluation(s), are given in the rightmost column.

We next turned to consider finite element models allowing for heterogeneous shear displacements. Beginning with a $1 \times 1 \times 1$ cube and the optimal material parameters from the homogeneous model as initial values, we computed optimal values for the $1 \times 1 \times 1$ case. This procedure was repeated for $N \times N \times N$ cubes with $N = 2, 4, 6, 8$, using the results of the previous optimization as the initial condition for the next case. The resulting parameter values are presented in Table 2, and the corresponding optimal stress-strain curves are shown in Figure 3.

We note that going from $N = 6$ to $N = 8$ using the transversely isotropic data and going from $N = 2$ to $N = 4$ using the orthotropic data does not change the first significant digit of any of the material parameters and therefore consider our finite element models to be sufficiently refined at this resolution. Indeed, for the orthotropic data, going from N = 2 to N = 4 does not change the first three significant digits.

3.3.2 Material parameter estimation using multi-start optimization

In this section, we present the results of using the multi-start method to estimate the optimal material parameters, rather than relying on a good initial guess. For the calculation of random initial guesses we set $P_{max} = 40$, cf. Section 2.3. This value is close to the largest material parameter found in Table 2. Note that this choice gives a conservative set of initial parameters for the optimization algorithm (low initial values) which in turn enhances the robustness of the procedure. We also set 60 as an upper bound for each material parameter value during the optimization. Without this upper bound we observed that many optimizations crashed or converged to suboptimal local minima.
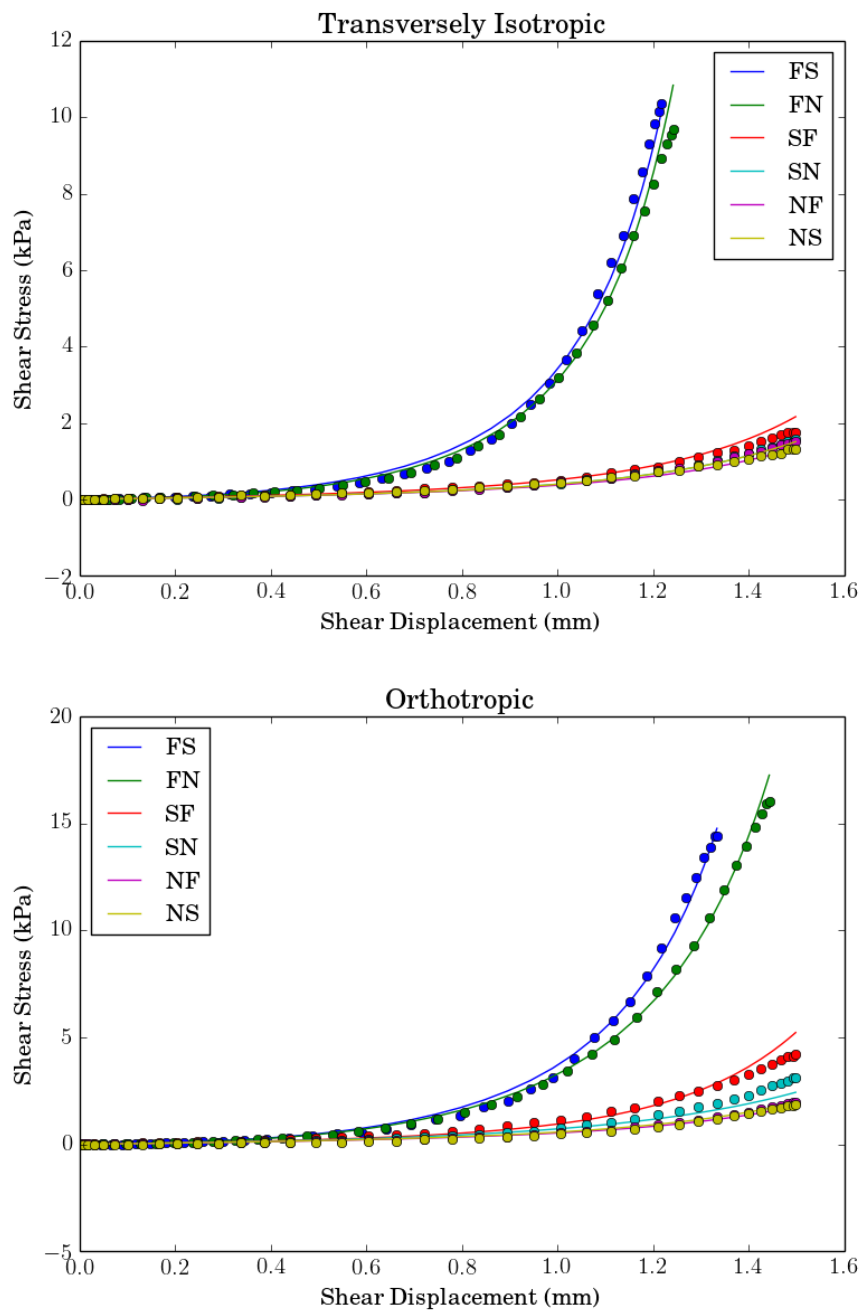
Fig. 3 Comparison of optimized model stress-strain curves with experimental data. The dots are interpolated experimental data at Gauss points, the solid lines show the output of the finite element models. An $N = 2$ cube was used in the plot labeled 'Orthotropic', while an $N = 6$ cube was used in the plot labeled 'Transversely Isotropic'.

Table 3 Results of fitting material parameters to the transversely isotropic and orthotropic data sets using the multi-start method. The rows labeled 'Best Fit' correspond to the optimizations with the lowest misfit value I, and the rows labeled 'Mean' and 'SD' give the mean and standard deviation of parameters not counting badly fitted sets (Table 4). The rows labeled '$N =$' are copied from Table 2 for easy reference.

	a (kPa)	b	a_f (kPa)	b_f	a_s (kPa)	b_s	a_{fs} (kPa)	b_{fs}	I (mN)
Transversely Isotropic									
$N = 6$	*0.732*	*7.362*	*21.511*	*40.020*	*0.010*	*0.010*	*0.209*	*13.862*	*2.827*
Best Fit	0.795	6.855	21.207	40.545	0.010	0.010	0.130	17.446	2.802
Mean	0.799	6.823	21.207	40.545	0.010	0.495	0.127	17.869	2.810
SD	0.027	0.214	0.038	0.091	0.000	1.103	0.023	2.758	0.034
Orthotropic									
$N = 2$	*1.041*	*6.553*	*29.371*	*15.982*	*1.741*	*0.010*	*0.118*	*23.294*	*4.563*
Best Fit	1.041	6.553	29.371	15.982	1.741	0.010	0.118	23.296	4.563
Mean	1.046	6.536	29.321	16.023	1.736	0.010	0.119	23.274	4.569
SD	0.013	0.020	0.089	0.289	0.229	0.030	0.000	0.012	0.475

Table 4 Badly fitting sets from multi-start optimization. The fit values, I, are significantly higher than those reported in Table 3.

	a (kPa)	b	a_f (kPa)	b_f	a_s (kPa)	b_s	a_{fs} (kPa)	b_{fs}	I (mN)
Transversely Isotropic									
	0.010	1.282	29.254	11.417	0.010	0.010	1.330	7.365	17.955
	1.068	0.010	37.315	9.722	0.104	0.010	3.322	1.902	13.094
Orthotropic									
	0.010	7.187	32.433	13.095	0.010	9.293	5.286	5.068	21.621

In each multi-start experiment, 30 random starting points were used. For the orthotropic data set, all 30 optimizations converged. For the transversely isotropic dataset, 27 optimizations converged. Those that did not converge were unable to numerically solve (4) at the point in parameter space that the optimizer was currently evaluating. The simulations were run with $N = 6$ for the transversely isotropic case and $N = 2$ for the orthotropic case.

The results of the multi-start optimizations show that all but three optimized parameter sets are very close to the previously obtained values. Table 3 shows the best fitting parameter sets, means, and standard deviations of the optimizations that fit reasonably well. We note that the means and best fits are very close to those obtained in Table 2, and that almost all the standard deviations are very small compared to the means. The three poorly fitted parameter sets that we obtained as local minima are included in Table 4 for completeness.

Table 5 Holzapfel-Ogden law parameter estimates from this and previous studies. Note that objective functional (I-) values are obtained using the orthotropic data used in this study, and not the data used in the studies the parameter estimates originate form.

Source	a (kPa)	b	a_f (kPa)	b_f	a_s (kPa)	b_s	a_{fs} (kPa)	b_{fs}	I (mN)
Holzapfel et al 2009	0.059	8.023	18.472	16.026	2.481	11.120	0.216	11.436	36.688
Goektepe et al 2011	0.496	7.209	15.193	20.417	3.283	11.176	0.662	9.466	30.208
Wang et al 2013	0.2362	0.810	20.037	14.154	3.7245	5.1645	0.4108	11.300	34.845
Current (Orthotropic Dataset)	1.041	6.553	29.371	15.982	1.741	0.01	0.118	23.294	4.563

3.3.3 Objective functional values for alternative material parameters

Several other studies [13, 16, 27] have used variants of the Dokos et al. 2002 shear data [9] to calibrate the Holzapfel and Ogden strain energy (2). These studies used homogenized deformation models for the optimization. In Table 5 we list the computed objective functional value of parameter sets originating from previous studies using the orthotropic dataset and finite element model ($N = 2$). The results indicate that our parameter set fits these data better than the previously computed ones.

3.4 Computational efficiency of the adjoint-based functional gradient

Adjoint solver efficiency may be measured by comparing the runtime of the adjoint and forward solves. Here, we examine the overall gradient efficiency in a similar manner. We consider the evaluation of the gradient of the objective functional (13), though in a reduced case with only a single shear mode included in the sum and a reduced forward solve consisting of a single nonlinear solver iteration. In this case, the forward and adjoint models each consist of a single linear solve in addition to a number of residual evaluations. For larger linear system sizes, the runtime of a linear solve is expected to dominate the runtime of assembly, and thus these forward and adjoint models are of roughly the same computational expense.

For this reduced case, we evaluated the adjoint-based gradient for a range of linear system sizes. For each system size, we calculated the gradient runtime ratio; that is, the runtime used by the evaluation of the gradient divided by the runtime of the forward solve. The resulting ratios are plotted in Figure 4. The curve indicates that the gradient run-time ratio gets close to the theoretically optimal value of 1 as we increase the system size.
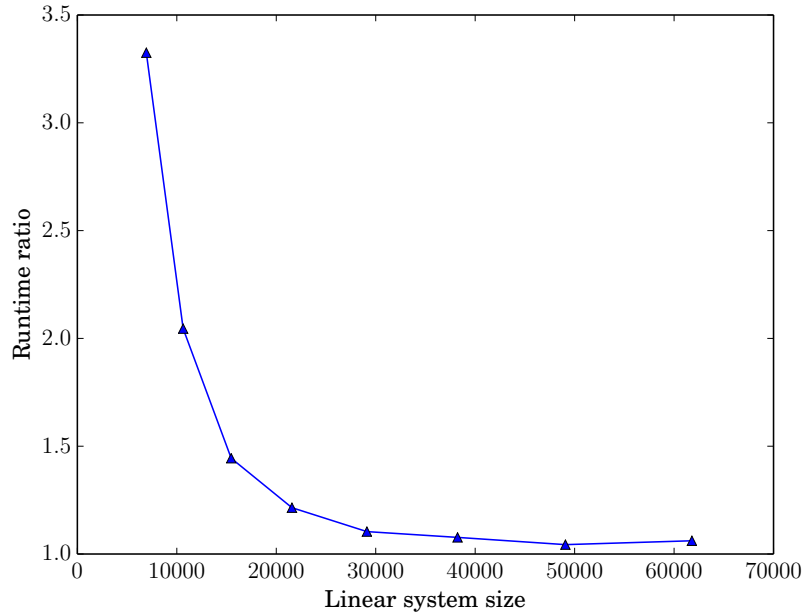
Fig. 4 Gradient efficiency: ratio of gradient evaluation runtime over single Newton iteration runtime for increasing linear system sizes.

4 Discussion

4.1 Choice of shearing experiment datasets

Of the six shearing experiment datasets, cf. Figure 1, we have used two for parameter estimation here. One of the reasons for this choice is an incompatibility of most of the datasets with assumptions made in the design of the strain energy functional (2). In particular, the strain energy (2) dictates an ordering of the shear mode stiffnesses in the case of a homogeneous shear displacement. This can easily be seen by modifying (5.23) – (5.28) of [16] to fit the invariants chosen in (2). Two of these orderings are

$$
\begin{aligned}
\tau_{FS} \geq \tau_{FN} \geq \tau_{NF} \\
\tau_{SF} \geq \tau_{SN} \geq \tau_{NF}
\end{aligned}
\tag{15}
$$

where τ_{ij} denotes a shear force in the direction of the mode ij.

Out of the six datasets, only one is consistent with these orderings, namely the 6th one, which was used here under the label transversely isotropic. In this dataset the stress-strain relationship is typical of a transversely isotropic material with a stiffer fiber direction. In several other cardiac mechanics simulation studies [11, 12, 19], the Holzapfel and Ogden energy functional (2) has been simplified to model transversely isotropic behavior by removing the terms

involving the invariants I_{4s}, I_{8fs}. For such a simplified model one could use the parameter estimates for a, b, a_f, b_f that we obtained from the Transversely Isotropic dataset.

However, the Holzapfel and Ogden model was originally proposed to model orthotropic behavior. This motivates also targeting a dataset displaying fully orthotropic behavior. In particular, dataset 2 in Figure 1 is such and compares well with Figure 6 of [9] and Figure 2 of [16]. By switching the SF and SN curves of Dataset 2 we were able to reinterpret this data in a way that is consistent with the interpretation in [16], and the shear stiffness orderings (15).

4.2 Comparison of optimal material parameter values

We have obtained two sets of material parameters: one corresponding to an orthotropic case and one corresponding to a transversely isotropic case. We observe that for both sets of material parameters, the b_s parameter essentially vanishes. For the Transversely Isotropic case, both a_s and b_s essentially vanish, which is in excellent agreement with the transversely isotropic stress-strain pattern.

Comparing the Orthotropic material parameter values to the previously published values in Table 5, we observe that the fit of our material parameters is significantly better, as expected. By using a finite element model we have been able to relax the homogeneous shearing angle assumption and more realistically model the motion of the cubes in the shearing experiment. We note that our material parameters differs from those previously published, and also that there is a significant variability in the parameter values previously reported.

4.3 Computing functional gradients in cardiac mechanics

Figure 4 demonstrates that the computational cost of the adjoint gradient computation is comparable to that of a single iteration of the nonlinear solution algorithm of (4) for larger system sizes. For smaller system sizes, the cost of symbolic computation and the cost of residual and Jacobian assembly contribute significantly yielding higher ratios – as expected. Wang et al.'s 2013 simulations of a human left ventricle in diastole use system sizes of approximately 100 000 degrees of freedom [27]. Given the trend in Figure 4, we can expect that the adjoint method and solver implemented in this work will continue to be efficient at this scale and beyond.

Comparatively, assuming the use of Newton's method for the solution of nonlinear systems, the evaluation of a finite difference gradient requires a linear system assembly and solve for each Newton iteration, and one nonlinear solve is required per component of the gradient. Counting the 8 parameters in the Holzapfel-Ogden model (2), and assuming a typical solution of the Euler-Lagrange equation (4) takes 6 Newton iterations, we can expect the

computational cost of finite difference gradient evaluation to be circa 48 times greater than that of the adjoint method.

In the optimization results of Table 2, we observed iteration counts of up to 178 for the optimization of 8 parameters using our gradient-based method. This compares favorably with the circa 7000 iterations needed to estimate 9 parameters using a global method in [29, Figure 5].

4.4 Implications for organ-scale image-based parameter estimation

Although we have tested our adjoint-based multi-start optimization method on the 2002 shear data of Dokos et al [9], we believe our methods will provide the biggest advantage in the case of optimizing cardiac model parameters in high spatial resolution at the organ scale to MRI or echocardiographic image data. This would allow for the proper modelling of regional differences in tissue stiffness, which is for example present in patients with post-infarct fibrosis.

In this paper we made the choice to use 30 multi-start points, and were able to obtain good results. However in the organ-scale case with patient image data it might not be clear how to choose between computational efficiency (less multi-start points) and robustness (more multi-start points). Possible solutions to this issue are the use of optimal stopping criteria [4] or more sophisticated local-global searches [14, 26].

5 Conclusion

In this work, we have presented a new application of efficient gradient-based optimization methods in the context of estimating cardiac hyperelastic material parameters from experimental data. In particular, we have demonstrated how an adjoint solution can greatly speed up the evaluation of functional gradients. These methods have produced two new sets of material parameter values that yield simulated stress-strain curves that fit closely to orthotropic and transversely isotropic shear data. For future parameter estimation studies using a local search algorithm, multi-start or a similar method should be used in order to avoid suboptimal minima.

References

1. Alnæs, M.S., Logg, A., Ølgaard, K.B., Rognes, M.E., Wells, G.N.: Unified form language: A domain-specific language for weak formulations of partial differential equations. ACM Transactions on Mathematical Software (TOMS) **40**(2), 9 (2014)

2. Augenstein, K.F., Cowan, B.R., LeGrice, I.J., Nielsen, P.M., Young, A.A.: Method and apparatus for soft tissue material parameter estimation using tissue tagged magnetic resonance imaging. Journal of biomechanical engineering **127**(1), 148–157 (2005)
3. Balay, S., Brown, J., Buschelman, K., Gropp, W., Kaushik, D., Knepley, M., McInnes, L.C., Smith, B., Zhang, H.: Petscc web page (2015). URL http://www.mcs.anl.gov/petsc
4. Boender, C.G.E., Kan, A.R.: Bayesian stopping rules for multistart global optimization methods. Mathematical Programming **37**(1), 59–80 (1987)
5. Byrd, R.H., Lu, P., Nocedal, J., Zhu, C.: A limited memory algorithm for bound constrained optimization. SIAM Journal on Scientific Computing **16**(5), 1190–1208 (1995)
6. Chabiniok, R., Moireau, P., Lesault, P.F., Rahmouni, A., Deux, J.F., Chapelle, D.: Estimation of tissue contractility from cardiac cine-mri using a biomechanical heart model. Biomechanics and modeling in mechanobiology **11**(5), 609–630 (2012)
7. Costa, K.D., Holmes, J.W., McCulloch, A.D.: Modelling cardiac mechanical properties in three dimensions. Philosophical transactions of the Royal Society of London. Series A: Mathematical, physical and engineering sciences **359**(1783), 1233–1250 (2001)
8. Delingette, H., Billet, F., Wong, K.C.L., Sermesant, M., Rhode, K., Ginks, M., Rinaldi, C.A., Razavi, R., Ayache, N.: Personalization of Cardiac Motion and Contractility From Images Using Variational Data Assimilation. Biomedical Engineering, IEEE Transactions on **59**(1), 20–24 (2012). DOI 10.1109/TBME.2011.2160347
9. Dokos, S., Smaill, B.H., Young, A.A., LeGrice, I.J.: Shear properties of passive ventricular myocardium. American Journal of Physiology-Heart and Circulatory Physiology **283**(6), H2650–H2659 (2002)
10. Farrell, P.E., Ham, D.A., Funke, S.W., Rognes, M.E.: Automated derivation of the adjoint of high-level transient finite element programs. SIAM Journal on Scientific Computing **35**(4), C369–C393 (2013)
11. Finsberg, H.N., Balaban, G., Sundnes, J., Odland, H.H., Rognes, M., Wall, S.T.: Mechanical imaging of dynamic patient stress patterns (2015). URL http://www.malt-meeting.net/2015/abstracts/balaban.pdf
12. Gjerald, S., Hake, J., Pezzuto, S., Sundnes, J., Wall, S.T.: Patient–specific parameter estimation for a transversely isotropic active strain model of left ventricular mechanics. In: Statistical Atlases and Computational Models of the Heart-Imaging and Modelling Challenges, pp. 93–104. Springer (2015)
13. Göktepe, S., Acharya, S., Wong, J., Kuhl, E.: Computational modeling of passive myocardium. International Journal for Numerical Methods in Biomedical Engineering **27**(1), 1–12 (2011)
14. Goldberg, D.E., Voessner, S.: Optimizing global-local search hybrids. Urbana **51**, 61,801 (1999)
15. Gunzburger, M.D.: Perspectives in flow control and optimization, vol. 5. Siam (2003)
16. Holzapfel, G., Ogden, R.W.: Constitutive modelling of passive myocardium: a structurally based framework for material characterization. Philosophical transactions. Series A, Mathematical, physical, and engineering sciences **367**(1902), 3445–75 (2009). DOI 10.1098/rsta.2009.0091. URL http://www.ncbi.nlm.nih.gov/pubmed/19657007
17. Hood, P., Taylor, C.: Navier-stokes equations using mixed interpolation. Finite element methods in flow problems pp. 121–132 (1974)
18. Jones, E., Oliphant, T., Peterson, P., et al.: SciPy: Open source scientific tools for Python (2001–). URL http://www.scipy.org/. [Online; accessed 2014-12-09]
19. Krishnamurthy, A., Villongco, C.T., Chuang, J., Frank, L.R., Nigam, V., Belezzuoli, E., Stark, P., Krummen, D.E., Narayan, S., Omens, J.H., et al.: Patient-specific models of cardiac biomechanics. Journal of computational physics **244**, 4–21 (2013)
20. Logg, A., Mardal, K.A., Wells, G.N., et al.: Automated Solution of Differential Equations By the Finite Element Method. Springer (2011)
21. Marchesseau, S., Delingette, H., Sermesant, M., Sorine, M., Rhode, K., Duckett, S.G., Rinaldi, C.a., Razavi, R., Ayache, N.: Preliminary specificity study of the Bestel-Clément-Sorine electromechanical model of the heart using parameter calibration from medical images. Journal of the mechanical behavior of biomedical materials **20**, 259–71 (2013). DOI 10.1016/j.jmbbm.2012.11.021. URL http://www.ncbi.nlm.nih.gov/pubmed/23499249

22. Schmid, H., Nash, M., Young, A., Röhrle, O., Hunter, P.: A computationally efficient optimization kernel for material parameter estimation procedures. Journal of biomechanical engineering **129**(2), 279–283 (2007)
23. Schmid, H., OCallaghan, P., Nash, M., Lin, W., LeGrice, I., Smaill, B., Young, A., Hunter, P.: Myocardial material parameter estimation-a nonhomogeneous finite element study from simple shear tests. Biomechanics and modeling in mechanobiology **7**(3), 161–173 (2008)
24. Schmid, H., Wang, Y., Ashton, J., Ehret, A., Krittian, S., Nash, M., Hunter, P.: Myocardial material parameter estimation-a comparison of invariant based orthotropic constitutive equations. Computer methods in biomechanics and biomedical engineering **12**(3), 283–295 (2009)
25. Sundar, H., Davatzikos, C., Biros, G.: Biomechanically-constrained 4d estimation of myocardial motion. In: Medical Image Computing and Computer-Assisted Intervention–MICCAI 2009, pp. 257–265. Springer (2009)
26. Tsai, F.T.C., Sun, N.Z., Yeh, W.W.G.: Global-local optimization for parameter structure identification in three-dimensional groundwater modeling. Water resources research **39**(2) (2003)
27. Wang, H., Gao, H., Luo, X., Berry, C., Griffith, B., Ogden, R., Wang, T.: Structure-based finite strain modelling of the human left ventricle in diastole. International journal for numerical methods in biomedical engineering **29**(1), 83–103 (2013)
28. Wang, V.Y., Lam, H.I., Ennis, D.B., Cowan, B.R., Young, A.a., Nash, M.P.: Modelling passive diastolic mechanics with quantitative MRI of cardiac structure and function. Medical image analysis **13**(5), 773–84 (2009). DOI 10.1016/j.media.2009.07.006. URL http://www.ncbi.nlm.nih.gov/pubmed/19664952
29. Wong, K.C., Sermesant, M., Rhode, K., Ginks, M., Rinaldi, C.A., Razavi, R., Delingette, H., Ayache, N.: Velocity-based cardiac contractility personalization from images using derivative-free optimization. Journal of the mechanical behavior of biomedical materials **43**, 35–52 (2015)
30. Xi, J., Lamata, P., Lee, J., Moireau, P., Chapelle, D., Smith, N.: Myocardial transversely isotropic material parameter estimation from in-silico measurements based on a reduced-order unscented kalman filter. Journal of the mechanical behavior of biomedical materials **4**(7), 1090–1102 (2011)
31. Zhu, C., Byrd, R.H., Lu, P., Nocedal, J.: Algorithm 778: L-bfgs-b: Fortran subroutines for large-scale bound-constrained optimization. ACM Transactions on Mathematical Software (TOMS) **23**(4), 550–560 (1997)